Threshold anomaly in $^{12}C+^{209}Bi$ scattering

S. Santra, P. Singh, S. Kailas, A. Chatterjee, A. Navin,* A. Shrivastava, A. M. Samant,† and K. Mahata
Nuclear Physics Division, Bhabha Atomic Research Centre, Mumbai - 400 085, India
(Received 3 February 1999; published 12 August 1999)

Elastic scattering angular distributions have been measured for the system $^{12}C+^{209}Bi$ at ten energies between 58.9 to 87.4 MeV. Optical model analysis of these, together with existing data at 118 MeV, using both phenomenological and microscopic models, shows a pronounced energy dependence of the optical potential. Fusion cross sections have been deduced, by a barrier penetration model and by subtracting the direct reaction contributions from the reaction cross sections. Threshold anomaly of the optical potential has been explained both by dispersion relation and by coupled reaction channel (CRC) calculations. The CRC calculations, including inelastic excitation and transfer channels, reproduce simultaneously the elastic, inelastic, and transfer angular distributions measured at 61.9, 63.9, and 87.4 MeV. Comparison of threshold anomaly results for ^{4}He, ^{11}B, $^{16}O+^{209}Bi$ systems along with the present case indicates that the degree of anomaly increases with the projectile mass. [S0556-2813(99)05808-2]

PACS number(s): 25.70.Bc, 25.70.Jj

I. INTRODUCTION

The dynamics of both elastic scattering and fusion are influenced by the couplings of the relative motion to nuclear intrinsic degrees of freedom of the colliding nuclei. The strong energy dependence of the real part of the optical potential near the Coulomb barrier (threshold anomaly), enhancement of fusion cross section, broadening of spin distribution at near barrier energies, the distribution of fusion barrier, etc., are the manifestations of such coupling effects. The apparently anomalous behavior (a bell shaped maximum) of the modulus of the real part of the optical potential is associated with the closing of the nonelastic channels as the energy drops below the Coulomb barrier. The nonelastic channel couplings can produce changes in the real potential through virtual excitations even below the thresholds where the corresponding channels are energetically closed [1]. The explicit coupled channel calculations including both inelastic scattering and transfer reactions, where the effective potential calculated to be the sum of an energy independent real bare potential and a derived polarization potential due to coupling effects, should be able to explain all the above effects.

The motivation of this work is to (i) measure the elastic, inelastic and transfer cross sections in $^{12}C+^{209}Bi$ scattering, (ii) investigate the energy dependence of the optical potential, (iii) explain the anomalous behavior, if any, in terms of a dispersion relation and coupled reaction channel (CRC) calculations, comparing the measured elastic, inelastic, and transfer data simultaneously. Systematic elastic scattering data and threshold anomaly results already exist for ^{4}He, ^{11}B, and ^{16}O on ^{209}Bi [2–4]. It is interesting to combine the data for these systems with $^{12}C+^{209}Bi$ to investigate the projectile dependence of the threshold anomaly. Although there are many heavy ion scattering systems [2–16], where the threshold anomaly has been observed, it is not very clear why some of the systems, like $^{7}Li+^{208}Pb$ [15] and $^{16}O+^{63}Cu$ [16] do show the anomalous behavior while others, like $^{6}Li+^{208}Pb$ and $^{16}O+^{65}Cu$ do not. Attempts have also been made to explain the threshold anomaly within the CRC framework for a few systems like, $^{16}O+^{208}Pb$ [17] and $^{16}O+^{58,60,62,64}Ni$ [18] but the anomaly is not yet well resolved, which may be because of the number of channels included in the CRC calculation are not sufficient. In none of the above systems the experimental transfer angular distributions are compared with the CRC results.

The target, ^{209}Bi, has a structure like ^{208}Pb (core)$\otimes 1h_{9/2}$ (single particle). There are seven and ten excited states of ^{209}Bi corresponding to 3^- and 5^- collective states of ^{208}Pb core respectively. It will be interesting to see the coupling effects on the entrance channel due to such a large number of inelastic channels which are coupled individually .

We have measured the elastic scattering angular distributions for $^{12}C+^{209}Bi$ system at several energies in the range of 58.9 to 87.4 MeV. Optical model analysis using both phenomenological and microscopic potentials, were performed to find the energy dependent potentials and are explained by a dispersion relation. Measured angular distributions for inelastic scattering for low lying vibrational states corresponding to 3^- of ^{208}Pb core and 1-neutron transfer corresponding to ground state (5^-) plus first excited state (4^+, 0.063 MeV) of ^{208}Bi, along with the elastic scattering data have been compared with the CRC results at three energies (E_{lab} = 61.9, 63.9 and 87.4 MeV).

Finally, we have compared the threshold anomaly observed experimentally in different systems (same target ^{209}Bi, but different projectiles), to determine the projectile dependence of this anomaly.

II. EXPERIMENTAL DETAILS

The elastic scattering measurements were carried out using ^{12}C beam at energies E_{lab} = 58.9, 59.9, 60.9, 61.9, 62.9,

*Present address: National Superconducting Cyclotron Laboratory, Michigan State University, East Lansing, MI 48823.
†Present address: I.N.F.N., Laboratory Nazionali di Legnaro, I-35020 Legnaro, Italy.

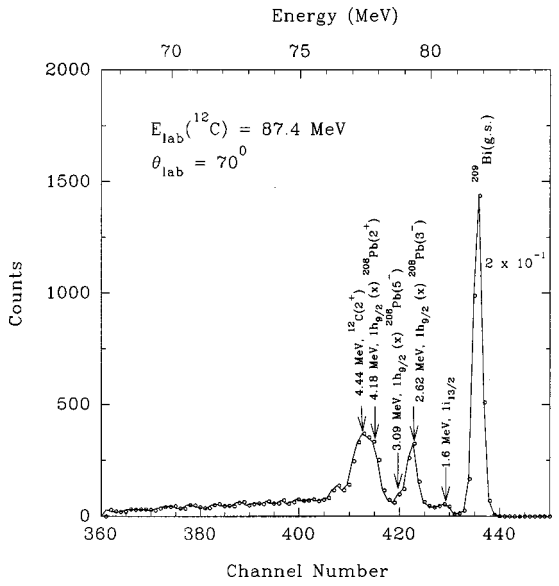

FIG. 1. Typical pulse height spectrum for ^{12}C scattered from ^{209}Bi at $E_{\rm lab}=87.4$ MeV.

63.9, 65.9, 69.9, 74.9 and 87.4 MeV, from the BARC-TIFR 14UD Pelletron at Mumbai. The targets used were in the form of self supporting foils of natural bismuth metal and were prepared using vacuum evaporation technique. The target thickness was determined by the energy loss method with an ^{241}Am α-source and estimated to be $\approx$300 μg/cm^2. Three telescopes of surface barrier detectors were set up on one of the movable arms inside a 1 m diameter scattering chamber for measuring the projectile like particles. A monitor detector was mounted on the other arm at 30° with respect to beam direction for obtaining the absolute cross sections assuming Rutherford scattering at this angle. The angular distributions were measured in the range $\theta_{\rm lab}=25°-173°$. The angular resolution was about 0.5°. The detector thicknesses were typically 20 to 45 μm for ΔE and 300 to 2000 μm for E-detectors. Proper gain matching in ΔE and E-signals led to a total energy resolution of $\approx$500 keV. It was possible to identify the charge and mass separated reaction products from ^{3}He to ^{14}C in 2D-spectrum of ΔE versus $E+\Delta E$ obtained from a fast-slow coincidence setup. A typical pulse height spectrum of ^{12}C band at 87.4 MeV bombarding energy is shown in Fig. 1. The single particle proton state $1i_{13/2}$ of ^{209}Bi at $E_x=1.608$ MeV is well resolved. The group of seven states with $E_x=2.49-2.741$ MeV formed by coupling of $1h_{9/2}$ single particle proton ground state with the 3^- collective excitation in ^{208}Pb appears to be a single broad peak with the centroid at 2.62 MeV. The other particle-core coupled states corresponding to 5^- and 2^+ of ^{208}Pb core vibrational states are centered at 3.09 and 4.18 MeV respectively. However, 4.18 MeV of ^{209}Bi could not be resolved from the 4.44 MeV of ^{12}C(2^+) state. In ^{13}C band the ground state (5^-) and the first excited state (4^+, 0.063 MeV) are unresolved, and therefore, the combined angular distributions have been extracted for 1n pick up. The differential elastic scattering cross sections, normalized to Rutherford cross sections, are shown in Fig. 2. The statistical errors on the elastic cross sections are typically $\approx$1% over the entire

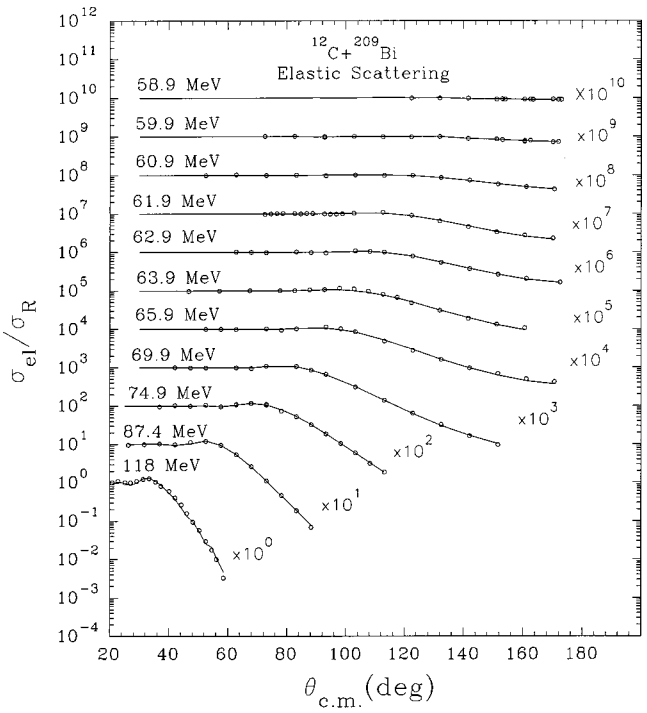

FIG. 2. Elastic scattering angular distributions for the ^{12}C $+^{209}$Bi system at different laboratory energies. The solid lines represent optical model fits to the data.

angular range at near and below barrier energies and for energies well above the barrier it is about 3% towards extreme backward angles. The errors remain within the size of the circle representing the data points. Significant differences are observed between the present data and those of Jin *et al.* [19] who have also reported elastic scattering data at $E_{\rm lab}=64.3$, 70.1, and 72.5 MeV. The values of σ_{el}/σ_R at backward angles for 64.3 and 70.1 MeV of Ref. [19] are larger by nearly a factor of 2 compared to the present work at nearby energies of 63.9 and 69.9 MeV, respectively. The reason for this difference is not clear. It may be pointed out that, due to use of energy degrader foils, the uncertainty in the beam energy values could be larger in their work. The ratio of the elastic to Rutherford, the inelastic cross sections corresponding to 2.62 MeV state and the transfer cross sections ^{209}Bi(^{12}C,^{13}C)^{208}Bi corresponding to the ground state of ^{13}C (with ground state plus first excited state of ^{208}Bi) at $E_{\rm lab}=61.9$, 63.9, and 87.4 MeV, are compared simultaneously with the CRC results.

III. OPTICAL MODEL ANALYSIS

A. Phenomenological analysis

The elastic scattering differential cross sections for all the above energies and the data available at 118 MeV [20], were analyzed consistently in the framework of optical model. A volume Woods-Saxon form of real and imaginary potential was used. The total potential is defined as

$$U(r)=V_c(r,r_c)-\{V(r)+iW(r)\}, \qquad (1)$$

TABLE I. Optical model (phenomenological) parameters from elastic scattering analysis.

E_{lab} (MeV)	V_0 (MeV)	r_0 (fm)	a_0 (fm)	W_0 (MeV)	r_w (fm)	a_w (fm)	σ_{reac} (mb)	χ^2/N
58.9	57.60	1.277	0.447	0.14	1.223	0.376	6.8	0.63
59.9	54.43	1.282	0.449	0.38	1.270	0.442	20.6	1.59
60.9	60.62	1.282	0.446	9.43	1.270	0.477	80.4	3.93
61.9	99.18	1.264	0.451	7.46	1.322	0.385	144	5.8
62.9	80.01	1.264	0.451	9.66	1.322	0.385	181	3.64
63.9	99.92	1.270	0.446	96.81	1.276	0.350	301	5.73
65.9	88.21	1.264	0.452	26.73	1.332	0.338	397	5.85
69.9	111.07	1.272	0.410	26.74	1.332	0.341	644	3.32
74.9	147.82	1.242	0.413	24.60	1.248	0.484	891	2.27
87.4	103.97	1.235	0.427	6.25	1.239	0.688	1372	2.93
118	66.12	1.235	0.427	5.46	1.239	0.697	2047	0.83

where $V(r)=V_0 f_0(r)$ and $W(r)=W_0 f_w(r)$. Here V_0 and W_0 are the strengths of the real and imaginary potentials, respectively, and the Woods-Saxon form factors are given by

$$f_x(r)=\frac{1}{(1+e^{(r-R_x)/a_x})}, \tag{2}$$

where $R_x=r_x(A_P^{1/3}+A_T^{1/3})$ with $x=0$ or w corresponding to real or imaginary parts of the potential respectively. A_P and A_T are the projectile and target masses, respectively. The Coulomb potential, $V_c(r,r_c)$ was taken as that due to a uniformly charged sphere of radius $R_c=r_c(A_P^{1/3}+A_T^{1/3})$ with r_c fixed at 1.3 fm. Optical model searches were carried out where all six parameters, i.e., strength, radius and diffuseness of real and imaginary potentials are allowed to vary to achieve the best fit. The parameters obtained from the fits to the experimental elastic scattering data at various energies are given in Table I, where N is the number of data points for respective energies. The values of the real potentials are calculated at strong absorption radius, $R_{sa}=12.9$ fm. The strong absorption radius can be computed from the formula for the distance of closest approach for Coulomb trajectories, i.e.,

$$R_{sa}=\frac{\eta}{k}\left[1+\left(1+\left(\frac{L_{1/2}}{\eta}\right)^2\right)^{1/2}\right], \tag{3}$$

where k is the wave number, η is the Sommerfeld parameter and $L_{1/2}$ is the partial wave for which the transmission coefficient is 0.5. The mean value for R_{sa} is estimated to be 12.9 fm. Using the data from Table I the values of the real and imaginary potentials are calculated at $r=12.9$ fm. and are plotted as a function of energy in Fig. 3. The errors on the potentials represent the values where χ^2 becomes twice of that at the central values, and are obtained by varying V_0 and W_0 on either side of its best fit value in the optical model fit to the elastic scattering data.

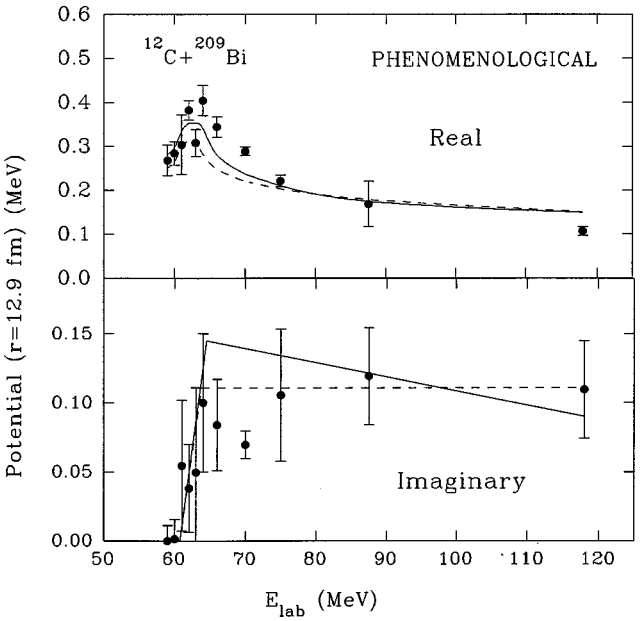

FIG. 3. Real and imaginary potentials at $r=12.9$ fm obtained from the phenomenological analysis. The solid and the dashed lines represent the two forms assumed for the imaginary potential. The corresponding real part has been obtained using the dispersion relation. (See text for details.)

B. Microscopic analysis

The elastic scattering data were also analyzed using a folding model potential [21]. The double folded potential for the system $^{12}C+^{209}Bi$ may be written as

$$V_F=\int\int d\mathbf{r}_1 d\mathbf{r}_2 \rho(\mathbf{r}_1)\rho(\mathbf{r}_2)v(\mathbf{r}_{12}), \tag{4}$$

where $\mathbf{r}$ is the separation of the centers of mass of the two colliding nuclei, v is the effective nucleon-nucleon interaction and the ρ's are point nucleon densities of ^{12}C and ^{209}Bi. The potentials were computed using the code DFPOT [22]. The interaction used was of the M3Y form [21], given by

$$v(r)=7999\frac{e^{-4r}}{4r}-2134\frac{e^{-2.5r}}{2.5r}+J_{00}\delta(r), \tag{5}$$

where the third term accounts for knock-on exchange with $J_{00}=-265$ MeV fm^3. For the densities ρ_1 and ρ_2, the charge density distributions obtained by fitting the electron scattering data and parametrized in the Fermi parabolic form,

$$\rho(r)=\frac{\rho_0(1+wr^2/c^2)}{1+e^{(r-c)/a}}, \tag{6}$$

with $c=2.355$ fm, $a=0.522$ fm, and $w=-0.149$ for ^{12}C and $c=6.75$ fm, $a=0.468$ fm, and $w=0$ for ^{209}Bi were used. The ρ_0 values were chosen so as to normalize the distribution to their respective charge numbers. The point nucleon densities were obtained from the charge densities after correcting for the finite size of the proton in the standard way [21], using the root mean square values of the radii,

TABLE II. Optical model (microscopic) parameters from elastic scattering analysis.

E_{lab} MeV	λ MeV	W_0 MeV	r_w fm	a_w fm	σ_{reac} mb	χ^2/N
58.9	2.28	1.58	1.233	0.453	5.4	0.75
59.9	2.56	7.33	1.270	0.442	24.8	2.26
60.9	2.96	14.55	1.270	0.452	79.2	4.03
61.9	3.05	4.31	1.322	0.503	149	1.97
62.9	2.94	16.04	1.323	0.379	191	5.41
63.9	2.84	4.92	1.329	0.561	300	5.37
65.9	2.86	4.90	1.332	0.472	379	5.75
69.9	2.63	7.99	1.394	0.348	644	3.32
74.9	2.55	17.77	1.320	0.404	886	2.22
87.4	2.19	11.77	1.320	0.411	1348	2.05
118	1.76	8.82	1.317	0.382	2012	1.04

$\langle r^2\rangle^{1/2}=2.455$ and 5.51 fm, of ^{12}C and ^{209}Bi, respectively. The potential used to carry out the fits to the elastic scattering data was of the form

$$U(r)=-\lambda V_F(r)-iW(r)+V_c(r). \tag{7}$$

In the analysis, the folded real potential $V_F(r)$, was allowed an overall adjustable normalization coefficient λ. The forms of the imaginary potential $W(r)$ and the Coulomb potential $V_c(r)$ were the same as that used in the phenomenological analyses of the data. The best fits were obtained by varying the parameters λ and $W(r)$. The parameters corresponding to best fits are listed in Table II. It can be seen that there exists a strong energy dependence in the values of λ.

The consistency between the real and imaginary potentials can be easily tested by a dispersion relation [23]. The nucleus-nucleus optical potential can be expressed in a local and angular momentum independent form as

$$V(r,E)=V(r)+\Delta V(r,E)+iW(r,E), \tag{8}$$

where $\Delta V(r,E)$ is the dispersive term arising from the energy dependent imaginary part $W(r,E)$ through the dispersion relation

$$\Delta V_{E_s}(r,E)=(E-E_s)\frac{P}{\pi}\int \frac{W(E')}{(E'-E_s)(E'-E)}dE', \tag{9}$$

where, P is the principal value of the integral, E_s is a suitable reference energy, and

$$\Delta V_{E_s}(r,E)=V(r,E)-V(r,E_s). \tag{10}$$

In principle, the real potential $V(r)$ must coincide with the microscopic potential and the sum $V(r)+\Delta V(r,E)$ with the empirical potential that reproduces the experimental elastic scattering. Figures 3 and 4 show the real and imaginary parts of the potentials calculated at the strong absorption radius $r=12.9$ fm using the parameters obtained from the phenomenological and microscopic analyses respectively, plotted as a function of bombarding energy. The imaginary potential is represented in the form of two straight line segments and the real potential calculated using dispersion relation is shown by the continuous curve. It can be seen that the optical model analyses (both phenomenological and folding model) clearly establishes the threshold anomaly for the present system.

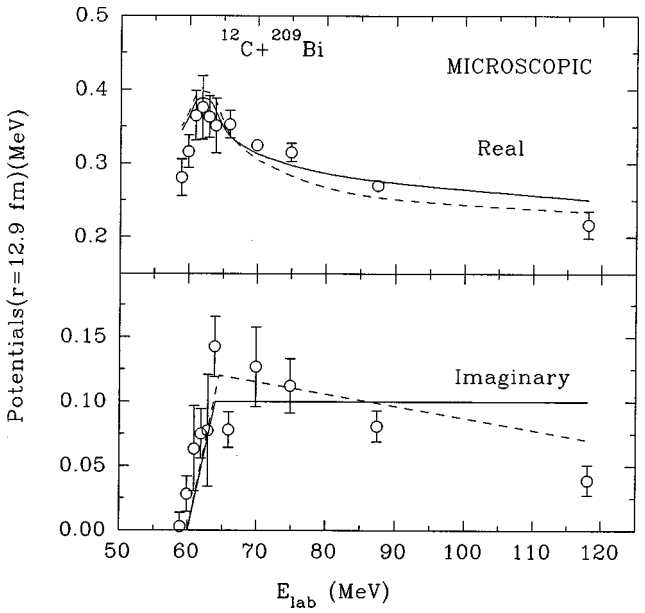

FIG. 4. Same as Fig. 3 but obtained from a microscopic analysis.

IV. FUSION CROSS SECTION

Fusion cross section (σ_F) can be calculated by a one dimensional energy dependent barrier penetration model (EDBPM) using the energy dependent fusion barrier parameters V_B and R_B, deduced from the sum of the real part of the optical potential and the Coulomb potential at each energy. The values of σ_F calculated using the expression

$$\sigma_F=\frac{R_B^2\hbar\omega}{2E}\ln\left[1+\exp\left(\frac{2\pi(E-V_B)}{\hbar\omega}\right)\right] \tag{11}$$

are shown as hollow circles in Fig. 5. The value of $\hbar\omega$ was determined to be 4.52 MeV. Using the same expression, the fusion cross sections were also calculated by the one dimensional barrier penetration model (1D-BPM) with energy independent barrier parameters. These parameters were taken to be same as that obtained for 87.4 MeV data, assuming that coupling effects are negligible at this energy compared to near barrier energies. The values of the fusion cross sections are shown in the figure as a dashed line. There is an enhancement in fusion cross sections calculated at the barrier and sub-barrier energies compared to the values obtained using the energy independent barrier.

It is also possible to calculate the fusion cross section (σ_F) if the reaction cross section (σ_R) is known, by subtracting the total quasielastic (inelastic and transfer) cross section, σ_{qe}^T from σ_R. The values of σ_{qe}^T are obtained by using the expression

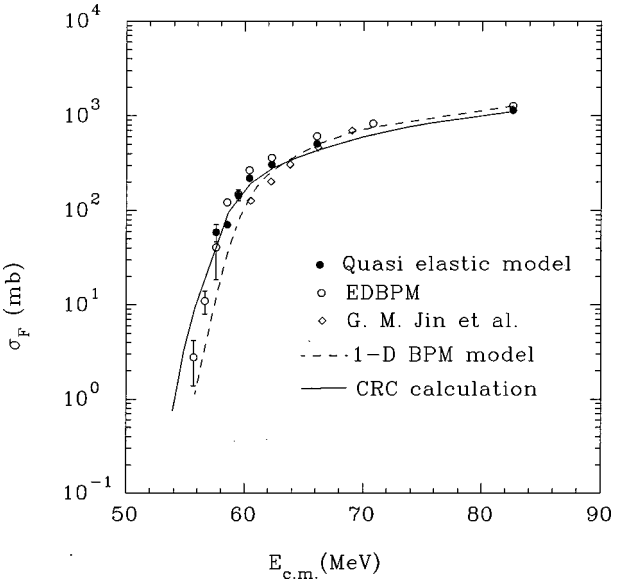

FIG. 5. Fusion cross sections obtained from quasielastic model and energy dependent barrier penetration model (EDBPM) are compared with those of Ref. [19]. The continuous line is obtained from CRC calculations.

$$\sigma_{qe}^{T}=\int_{0}^{2\pi}d\phi\int_{\theta_F}^{\pi}\sigma_{qe}(\theta)\sin(\theta)d\theta, \tag{12}$$

where θ_F is the angle corresponding to the maximum value-(Fresnel peak) of $\sigma_{el}(\theta)$. Figure 5 compares the fusion cross sections (σ_F) obtained by these two methods with the experimental fusion cross sections measured by Jin *et al.* [19]. The data of Jin *et al.* are in general smaller than the ones deduced here. From comparison of our data (both elastic and fusion) with [19], it is estimated that the actual energy corresponding to their data could be less by ≈ 1 MeV.

These fusion cross sections are an additional constraint for the CRC calculations. The fusion cross sections obtained by CRC calculations are represented by the solid line. These values at energies below the barrier are little more compared to those obtained by barrier penetration model.

V. CRC CALCULATIONS FOR $^{12}C+^{209}Bi$

In order to explain the threshold anomaly, the CRC calculations for the present system were performed with the program FRESCO [24]. The channels included in the CRC calculations are those expected to have significant couplings to the elastic channel, and are shown schematically in Fig. 6.

The inelastic states in ^{209}Bi arising due to collective excitations alone have been included in the present CRC calculations. There are 19 inelastic channels coupled to the entrance channel, out of which, 17 channels are corresponding to the inelastic states generated due to coupling of the single proton ($1h_{9/2}$) g.s. to 3^- (2.62 MeV) and 5^- (3.09 MeV) states of ^{208}Pb core. The last inelastic channel corresponds to the projectile excited state (2^+) at 4.44 MeV. Since the coupling strength of the inelastic states corresponding to $1h_{9/2} \otimes {}^{208}\mathrm{Pb}(2^+)$ with the centroid at 4.18 MeV is less compared

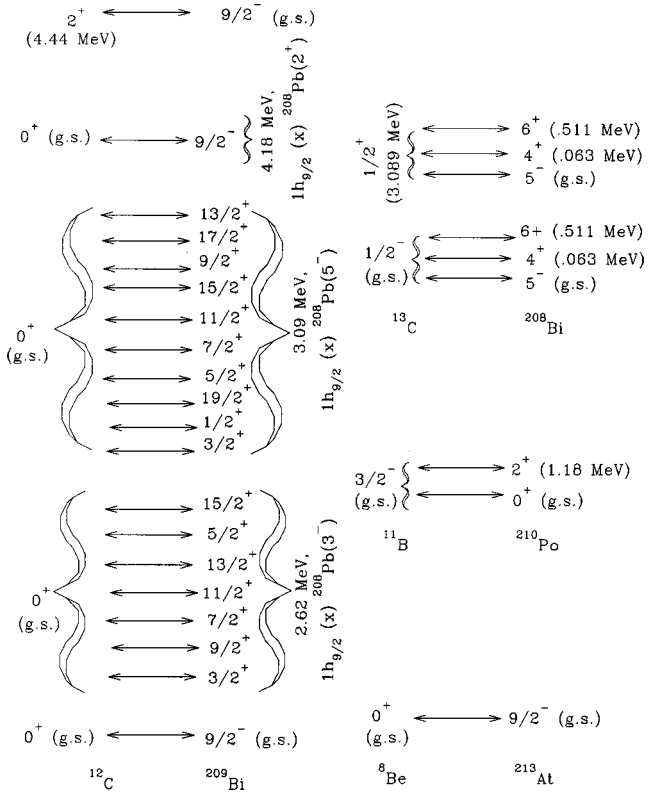

FIG. 6. Coupling scheme used for the CRC calculations. The spacing between different channels included are not to energy scale.

to 3^- and 5^-, it is decided to attribute all the strengths of these five states to a single state ($9/2^-$) to reduce the space and time requirement for computation. Moreover we are interested to see the coupling effects due to some of the important channels rather than the individual angular distributions for all the states. The single particle state ($2f_{7/2}$) at 0.896 MeV which is weakly excited as compared to 3^- and 5^- collective excited states has not been included in the CRC calculations. The $1i_{13/2}$ single particle level at 1.608 MeV is known to have a large admixture of $13/2^+$ member of 2.62 MeV septuplet [25]. In essence, the contribution of this state is already included in the fragmented states centered around 2.62 MeV. Three transfer partitions included in the calculations, correspond to one neutron pickup, one proton stripping and a single equivalent α transfer channel. All the nonelastic channels are coupled to the entrance channel only. The inelastic states were treated as collective (vibrational) states and their form factors were chosen to be the derivatives of the potentials. The β values [26] and the deformation lengths are listed in Table III. Different Coulomb and nuclear reduced deformation lengths were calculated for each possible transition corresponding to the same collective (vibrational) states. The spectroscopic factors (C^2S values) used in the calculations for nucleon transfer channels were taken from the literature [27–31] and are listed in the Table IV. The strength of the α transfer was adjusted to get the cross section of the same order as was measured [19] at 72.5 MeV.

The optical potentials in the elastic and inelastic channels were assumed to be identical and consisted of the bare,

TABLE III. β's and deformation lengths for inelastic (vibrational) states used in the CRC calculations.

Nucleus	State	Energy (MeV)	β	Deformation length (fm)
^{12}C	2^+	4.44	0.592	1.549
^{209}Bi	3^-	2.62	0.122	0.828
^{209}Bi	5^-	3.09	0.0802	0.544
^{209}Bi	2^+	4.18	0.05	0.340

double folded real potential and a Woods-Saxon squared imaginary potential of depth 50 MeV with a radius parameter of 1.0 fm and a diffuseness parameter of 0.4 fm. The imaginary term serves to absorb flux which has penetrated inside the Coulomb barrier and not on the surface. Thus it is necessary to couple explicitly all nonelastic modes which occur at nuclear surface. The parameters of the bare potential in the entrance channel were taken to be same as the real part of the optical potential obtained from microscopic analyses for 87.4 MeV data, which is equal to $\lambda(=2.19)$ times the value of the double folded potential.

For transfer partitions, the real potentials were calculated using the semiemperical parametrization of folding model potentials given by Broglia and Winther [32]

$$U_n(r) = -31.67\frac{R(A_1)R(A_2)}{R(A_1)+R(A_2)} \times\left[1+\exp\left(\frac{r-R(A_1,A_2)}{a}\right)\right]^{-1} \text{MeV}, \quad (13)$$

where, $R(A)=1.233A^{1/3}-0.98A^{-1/3}$ fm and $R(A_1,A_2)=R(A_1)+R(A_2)+\Delta R$ fm with the diffuseness parameter set to $a=0.63$ fm and the free parameter $\Delta R=0.2$ fm. The imaginary parts were of Woods-Saxon squared form, of 10 MeV, radius parameter 1.0 fm and diffuseness parameter 0.4 fm. The potentials binding the transferred particles were of Woods-Saxon form, with radius $1.2A^{1/3}$ fm and diffuseness 0.6 fm, their depths being automatically adjusted to obtain the required binding energies.

TABLE IV. Spectroscopic factors (C^2S values) for transfer states.

Nucleus	State	Energy (MeV)	C^2S
^{13}C	$\frac{1}{2}^-$	0.00	1.15
^{13}C	$\frac{1}{2}^+$	3.089	0.95
^{208}Bi	5^+	0.00	1.07
^{208}Bi	4^+	0.063	0.87
^{208}Bi	6^+	0.511	1.30
^{11}B	$\frac{3}{2}^-$	0.00	2.98
^{210}Po	0^+	0.00	1.00
^{210}Po	2^+	1.1814	1.00
^{8}Be	0^+	0.00	0.48
^{213}At	$\frac{9}{2}^-$	0.00	1.69

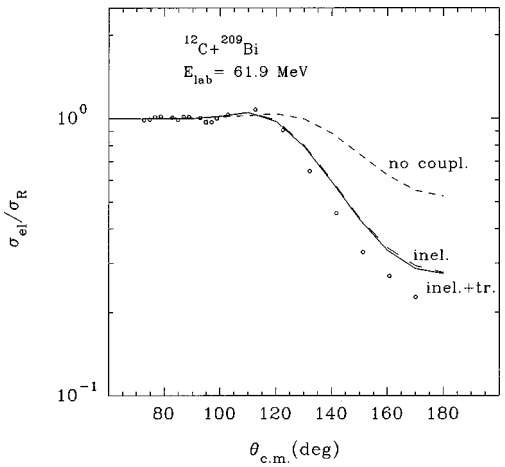

FIG. 7. Effect on elastic scattering due to the coupling of other nonelastic channels. In the figure the calculations with inelastic plus transfer, only inelastic and no coupling are represented as solid, long-dashed, and short-dashed curves, respectively.

The CRC results for elastic and nonelastic cross sections were compared with the experimental data at three selected energies(two near barrier and one much above the barrier energies). The effect of couplings of various nonelastic channels on the elastic cross section at 61.9 MeV is shown in Fig. 7. The final calculations with all significant channels reproduce the measured data reasonably well at all the energies and are shown in Fig. 8. The above calculations are done using the same set of channels and coupling parameters and without introducing any energy dependent parameters. It may be noted that we have used the structure information available in the literature and predicted the cross sections instead of trying to fit the experimental data. The effective potential [17] which was obtained by adding the polarization potential to the bare potential evaluated at $r=12.9$ fm is compared in Fig. 9 with the energy dependent potentials obtained from the microscopic optical model analyses.

VI. PROJECTILE DEPENDENCE OF THRESHOLD ANOMALY

Several systems (^{4}He, ^{11}B, ^{16}O+^{209}Bi) studied [2–4], with different projectiles but using the same target, having pronounced threshold anomaly, are compared including the present system (^{12}C+^{209}Bi) to see the degree of barrier shift with projectile mass. The fusion barrier parameters at different energies for each system are obtained by adding the Coulomb potential to the real part of the phenomenological potential. The maximum reduction in barrier heights, ΔV_B, arising due to the threshold anomaly compared to that obtained at highest available energies, deduced for ^{4}He, ^{11}B, ^{12}C, and ^{16}O+^{209}Bi systems, are 0.28 ± 0.06, 0.54 ± 0.12, 1.56 ± 0.31, and 1.88 ± 0.40 MeV respectively. The product of ΔV_B and the barrier radius, R_B, are shown as open circles in Fig. 10. It can be seen that these values increase with the mass of the projectile. This observation is consistent with the expectation that the coupling effects should increase with the mass of the projectile, which will be clear from the following discussions.

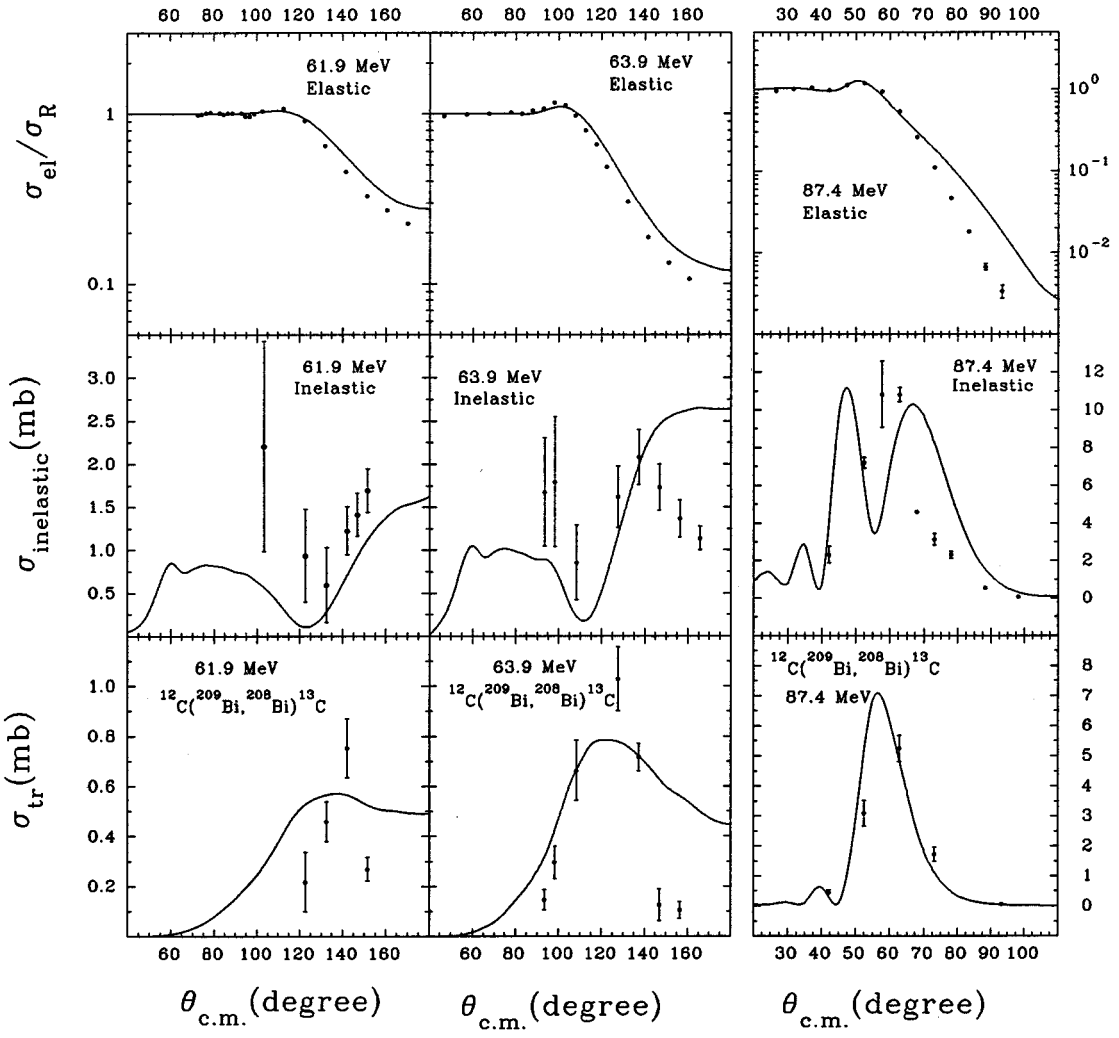

FIG. 8. Results from CRC calculations for elastic, inelastic (Bi 3^-) and $1n$ transfer corresponding to g.s. (5^-) plus first excited state (4^+, 0.063 MeV) of ^{208}Bi; angular distributions are compared with the experimental values at 61.9, 63.9, and 87.4 MeV.

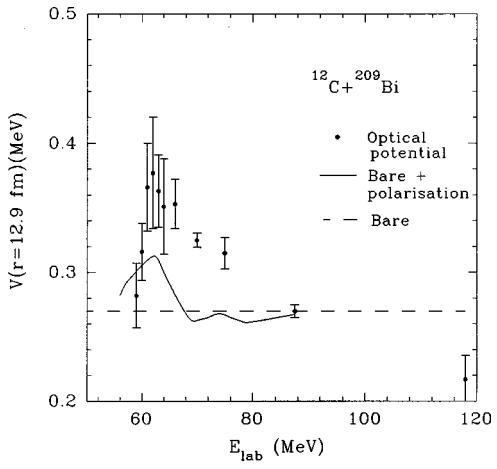

FIG. 9. Effective (bare+polarization) potential obtained from the CRC calculations (solid line). Filled circles are the real potentials obtained from the microscopic analysis. Dashed line is the bare potential.

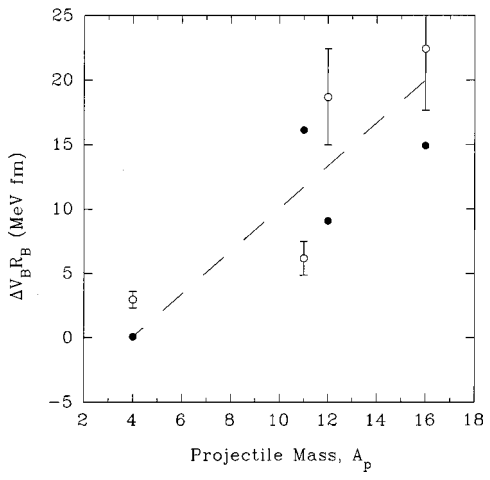

FIG. 10. The variation of the product of ΔV_B (barrier shift due to threshold anomaly) and R_B (barrier radius) with projectile mass is shown as hollow circles. Filled circles correspond to the calculated $\Delta V_{\rm pol} R_B$ values. The dashed line is to guide the eye.

The average reduction in barrier, ΔV_B, produced only by the deformations of the target and projectile is to a first order given by [33]

$$\Delta V_B = V_B \sqrt{\left[\left(\sum_\lambda \beta_\lambda^p\right)\frac{R_p}{R_B}\right]^2 + \left[\left(\sum_\lambda \beta_\lambda^t\right)\frac{R_t}{R_B}\right]^2}, \quad (14)$$

where R_p and R_t are the radii of the projectile and target, respectively, and λ is the multipolarity of the deformation. In the present case, the target is same. Therefore, the above equation can be rewritten as

$$\Delta V_B R_B = \sqrt{[C_1(p,\lambda)A_p^{2/3} + C_2]}V_B, \quad (15)$$

where $C_1 = (\Sigma_\lambda \beta_\lambda^p)^2$, is a function of projectile deformation parameters, A_p is the projectile mass, and $C_2 = (\Sigma_\lambda \beta_\lambda^t)^2 R_t^2$, is a constant. Since, V_B increases with projectile charge, Z_p, the right hand side terms should increase with mass and charge of the projectile, provided, the β_λ^p values are comparable.

Apart from the inelastic channels, the contributions to the barrier shift will also come from the transfer channels. In addition to the neutron transfer, since there will be more transfer channels possible for heavier projectiles corresponding to the stripping of their protons which are more favorable at lower energies than the pick up channels, the number of channels coupled will be more. If there are N inelastic plus transfer channels and we assume that couplings to the ground state (V_{cpl}) are similar for each channel and neglect any other cross channel couplings, it can be shown that the barrier is reduced by $\sqrt{N}V_{cpl}$ at lower barrier energies [34]. The barrier shift associated with each channel is also given by $\lambda^- = \frac{1}{2}(-Q_0^2 - \sqrt{Q_0^2 + 4f^2})$ [35], where f is the coupling strength and Q_0 is Q-value of the channel. Neglecting the cross couplings the polarization potentials arising due to each channel are additive and hence the barrier reduction will increase with the number of channels. This implies increase of $\Delta V_B R_B$ with A_p. In addition, there will also be contribution to the threshold anomaly arising due to the specific structure of the projectile concerned.

The CRC calculations are performed to derive the effective polarization potentials, $\Delta V_{\rm pol}$, for all the above four systems including only the inelastic channels. Three vibrational states (3^-, 5^-, and 2^+) of the target, 3^- of ^{16}O, 2^+ of ^{12}C and ^{11}B and no projectile excitation for ^{4}He were included in the calculations. The product of $\Delta V_{\rm pol}$ and R_B are represented by the filled circles in Fig. 10 for comparison. It is interesting to note that the deduced $\Delta V_B R_B$ values increase with A_p as expected from simple considerations.

VII. CONCLUSIONS

Systematic elastic scattering measurements are reported for the system ^{12}C+^{209}Bi in the energy range of 58.9 to 87.4 MeV. The optical model (both phenomenological and microscopic) analysis of the data at all the above energies and the data available in the literature at 118 MeV [20], has clearly established the *threshold anomaly* for this system and the same has been explained using the dispersion relation. The fusion cross sections obtained by energy dependent barrier penetration model and quasi elastic model are in good agreement and show an enhancement at sub-barrier energies compared to those obtained from the energy independent one dimensional barrier penetration model. The results of the CRC calculations, which included a large number of inelastic and transfer channels, are consistent with the observed threshold anomaly. The comparison of the threshold anomaly seen in various systems (^{4}He, ^{11}B, ^{12}C, and ^{16}O+^{209}Bi) shows that the barrier shift (reduction) increases with the projectile mass as expected.

ACKNOWLEDGMENTS

The authors thank the staff of the BARC-TIFR Pelletron facility, Mumbai, for the smooth operation of the accelerator during the experiments carried out for this work.

[1] C. Mahaux, H. Ngo, and G. R. Satchler, Nucl. Phys. **A449**, 354 (1986).
[2] P. Singh, S. Kailas, A. Chatterjee, S. S. Kerekatte, A. Navin, A. Nijasure, and B. John, Nucl. Phys. **A555**, 606 (1993).
[3] P. Singh, A. Chatterjee, S. K. Gupta, and S. S. Kerekatte, Phys. Rev. C **43**, 1867 (1991).
[4] A. Shrivastava, S. Kailas, P. Singh, A. Chatterjee, A. Navin, A. Samant, V. Ramdev Raj, S. Mandal, S. K. Dutta, and D. K. Awasthi, Nucl. Phys. **A635**, 411 (1998).
[5] M. A. Nagarajan, C. C. Mahaux, and G. R. Satchler, Phys. Rev. Lett. **54**, 1136 (1985).
[6] B. R. Fulton, D. W. Banes, J. S. Lilley, M. A. Nagarajan, and I. J. Thompson, Phys. Lett. **162B**, 55 (1985).
[7] D. Abriola, A. A. Sonzogni, M. di Tada, A. Etchegoyen, M. C. Etchegoyen, J. O. Farnandez Niello, S. Gill, A. O. Macchiavelli, A. J. Pacheco, R. Piegaia, and J. E. Testoni, Phys. Rev. C **46**, 244 (1992).
[8] H. Leucker, K. Becker, K. Blatt, W. Korsch, W. Luck, H. G. Volk, D. Fick, R. Butsch, H. J. Jansch, H. Reich, and Z. Moroz, Phys. Lett. B **223**, 277 (1989).
[9] B. Bilwes, R. Bilwes, J. Diaz, and J. L. Ferrero, Nucl. Phys. **A449**, 519 (1986).
[10] J. Diaz, J. L. Ferrero, J. A. Ruiz, B. Bilwes, and R. Bilwes, Nucl. Phys. **A494**, 311 (1989).
[11] R. J. Tighe, J. J. Vega, E. Aguilera, G. B. Liu, A. Morsad, J. J. Kolata, S. H. Fricke, H. Esbensen, and S. Landowne, Phys. Rev. C **42**, 1530 (1990).
[12] A. M. Stefanini, A. Tivelli, G. Montagnoli, D. R. Napoli, D. Bonamini, S. Beghini, F. Scarlassara, F. Soramel, C. Signorini, A. De Rosa, G. Inglima, M. Sandoli, G. Cardella, M. Papa, and F. Rizzo, Phys. Rev. C **41**, 1018 (1990).
[13] J. M. Barrigon, A. Baeza, J. L. Ferrero, J. C. Pacheco, B. Bilwes, and R. Bilwes, Nucl. Phys. **A545**, 720 (1992).
[14] M. E. Brandon, J. R. Alfaro, A. Menchaca-Rocha, J. Gomez

del Campo, G. R. Satchler, P. H. Stelson, H. J. Kim, and D. Shapira, Phys. Rev. C **48**, 1147 (1993).
[15] N. Keeley, S. J. Bennett, N. M. Clarke, B. R. Fulton, G. Tungate, P. V. Drumm, M. A. Nagarajan, and J. S. Lilley, Nucl. Phys. **A571**, 326 (1994).
[16] D. Pereira, G. Ramirej, O. Sala, L. C. Chamon, C. A. Rocha, J. C. Acquadro, and C. Tenreiro, Phys. Lett. B **220**, 347 (1989).
[17] I. J. Thompson, M. A. Nagarajan, J. S. Lilley, and M. J. Smithson, Nucl. Phys. **A505**, 84 (1989).
[18] N. Keeley, J. S. Lilley, and J. A. Christley, Nucl. Phys. **A603**, 97 (1996).
[19] Jin Gen-Ming, Xie Yuan-Xiang, Zhu Yong-Tai, Shen Wen-Ging, Sun Xi-Jun, Guo Jun-Sheng, Liu Guo-Xing, Yu Ju-Sheng, Shun Chi-Chang, and J. D. Garrett, Nucl. Phys. **A349**, 285 (1980).
[20] A. M. Friedman and R. H. Siemssen, Phys. Rev. C **6**, 2219 (1972).
[21] G. R. Satchler and W. G. Love, Phys. Rep. **55**, 183 (1979).
[22] J. Cook, Comput. Phys. Commun. **25**, 125 (1982).
[23] G. R. Satchler, Phys. Rep. **199**, 147 (1991).
[24] I. J. Thompson, Comput. Phys. Rep. **7**, 167 (1988).
[25] W. T. Wagner, G. M. Crawley, and G. R. Hammerstein, Phys. Rev. C **11**, 486 (1975).
[26] T. P. Cleary, Nelson Stein, and P. R. Maurenzig, Nucl. Phys. **A232**, 287 (1974).
[27] L. Jarczyk, B. Kamys, Z. Rudy, A. Strazalkowski, and H. Wita*l*a, Phys. Rev. C **28**, 700 (1983).
[28] G. M. Crawley, E. Kashy, W. Lanford, and H. G. Blosser, Phys. Rev. C **8**, 2477 (1973).
[29] S. Cohen and D. Kurath, Nucl. Phys. **A101**, 271 (1967).
[30] R. Groleau, W. A. Lanford, and R. Kouzes, Phys. Rev. C **22**, 440 (1980).
[31] K. Umeda, T. Yamaha, T. Suchiro, K. Takimoto, R. Wada, E. Takada, S. Shimoura, A. Sakaguchi, S. Murakami, M. Fukada, and Y. Okuma, Nucl. Phys. **A429**, 88 (1984).
[32] R. A. Broglia and A. Winther, *Heavy Ion Reactions*, Parts I and II (Addison-Wesley, Redwood City, CA, 1991).
[33] S. Gil and D. E. Digregorio, Phys. Rev. C **57**, R2826 (1998).
[34] M. Dasgupta, A. Navin, Y. K. Agarwal, C. V. K. Baba, H. C. Jain, M. L. Jhingan, and A. Roy, Nucl. Phys. **A539**, 351 (1992).
[35] C. H. Dasso, S. Landowne, and A. Winther, Nucl. Phys. **A405**, 381 (1983), **A407**, 221 (1983).